Deng *et al. Alzheimer's Research & Therapy* (2025) 17:104
https://doi.org/10.1186/s13195-025-01734-6

Alzheimer's Research &
Therapy

RESEARCH **Open Access**

tRF$^{Ala\text{-}AGC\text{-}3\text{-}M8}$ attenuates neuroinflammation and neuronal damage in Alzheimer's disease via the EphA7-ERK$_{1/2}$-p70S6K signaling pathway

Zihao Deng[1,2], Yudi Li[1], Wenjun Chi[1,3], Wanzhou Zhang[1], Fangming Li[5*†] and Li Ling[1,4*†]

Abstract

Background Alzheimer's disease (AD) is a chronic, progressive neurodegenerative disorder clinically characterized by memory decline, cognitive dysfunction, language impairment, deterioration of visuospatial skills, and personality changes. Pathologically, AD is marked by the deposition of β-amyloid (Aβ) plaques in the brain, the formation of neurofibrillary tangles, and progressive neuronal loss. Recent research has highlighted transfer RNA (tRNA)-derived small RNAs (tsRNAs) as crucial regulators in various biological processes; however, their roles in the pathophysiology of AD remain largely unexplored. The erythropoietin-producing hepatocellular (Eph) receptor family has recently drawn attention in the study of neurodegenerative diseases due to their role in regulating critical processes, including cell migration, neural development, angiogenesis, and tumor formation. This study aimed to investigate specific tsRNAs associated with AD by performing RNA sequencing on the cortex of APP/PS1 transgenic mice and to explore the relationship between tsRNAs and their target genes within the Eph receptor family, thereby elucidating insights into the specific regulatory functions of these molecules.

Methods Eight-month-old male C57BL/6 and APP/PS1 transgenic mice were used in the study. BV-2 and HT22 cells were cultured and treated with Aβ$_{25\text{-}35}$ at concentrations ranging from 0 μM to 40 μM. RNA was extracted from cortical tissues, and tRNA-derived fragments were analyzed after pre-treatment to remove RNA modifications. Differential expression of tRFs and tiRNAs was identified through sequencing, followed by bioinformatics analysis of target genes using TargetScan and miRanda. Transfection of BV-2 and HT22 cells with EphA7-siRNA and tRF$^{Ala\text{-}AGC\text{-}3\text{-}M8}$-mimic was conducted, and their interaction was validated using dual-luciferase reporter assays. Protein expression levels were assessed by western blotting and immunofluorescence. Statistical analyses were performed using R and GraphPad Prism, with significance set at $p < 0.05$.

---

†Li Ling and Fangming Li contributed equally to this work.

*Correspondence:
Fangming Li
lifly050413@163.com
Li Ling
linglirabbit@163.com

Full list of author information is available at the end of the article

© The Author(s) 2025. **Open Access** This article is licensed under a Creative Commons Attribution-NonCommercial-NoDerivatives 4.0 International License, which permits any non-commercial use, sharing, distribution and reproduction in any medium or format, as long as you give appropriate credit to the original author(s) and the source, provide a link to the Creative Commons licence, and indicate if you modified the licensed material. You do not have permission under this licence to share adapted material derived from this article or parts of it. The images or other third party material in this article are included in the article's Creative Commons licence, unless indicated otherwise in a credit line to the material. If material is not included in the article's Creative Commons licence and your intended use is not permitted by statutory regulation or exceeds the permitted use, you will need to obtain permission directly from the copyright holder. To view a copy of this licence, visit http://creativecommons.org/licenses/by-nc-nd/4.0/.

Results We identified for the first time that EphA7 expression is upregulated in aggregated microglia and neuronal cells in the dentate gyrus region of the hippocampus, with increased phosphorylation of $ERK_{1/2}$ and p70S6K in AD. This upregulation occurred following the downregulation of $tRF^{Ala\text{-}AGC\text{-}3\text{-}M8}$ due to Aβ stimulation and was confirmed via in vitro experiments. By inhibiting EphA7 expression and increasing $tRF^{Ala\text{-}AGC\text{-}3\text{-}M8}$ expression, we suppressed the $ERK_{1/2}$-p70S6K signaling pathway in BV-2 and HT22 cells. This intervention alleviated neuronal damage and tau hyperphosphorylation in HT22 cells and reduced the M1-type polarization state of BV-2 cells induced by $Aβ_{25\text{-}35}$ (see Graphical Abstract).

Conclusions This study clarifies the specific role of $tRF^{Ala\text{-}AGC\text{-}3\text{-}M8}$ in AD pathology and offers a promising target for therapeutic interventions.

Keywords tRFAla-AGC-3-M8, Alzheimer's disease, EphA7, Neuroinflammation, tsRNA, Microglia, $ERK_{1/2}$, p70S6K

Graphical Abstract

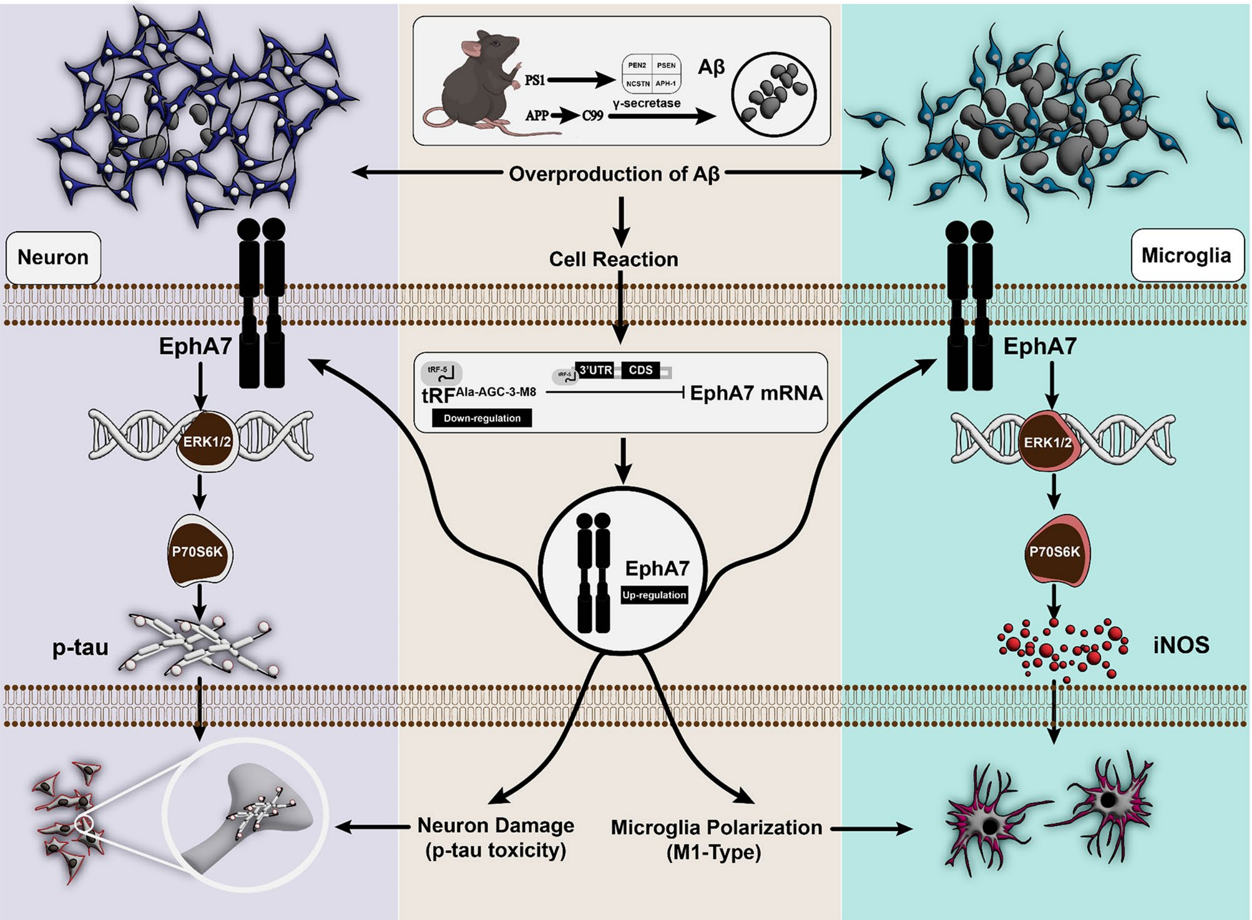

Background

Alzheimer's disease (AD) is a progressive, neurodegenerative disorder and the most common type of dementia among older adults. Its pathological features include the formation of β-amyloid (Aβ) plaques and neurofibrillary tangles (NFTs). Aβ aggregation activates microglia, triggering an inflammatory response. Early in the disease, microglia can recognize and clear abnormal Aβ aggregates. However, as AD progresses, microglia may polarize to the M1-type, releasing excessive pro-inflammatory factors (such as tumor necrosis factor-α and interleukin [IL]-1β) and neurotoxic substances [1–3]. These factors negatively affect nearby neurons, exacerbating neuroinflammation. Tau, a microtubule-associated protein, normally supports microtubule structure in neurons and can become hyperphosphorylated. This hyperphosphorylation impairs its ability to bind to microtubules, leading to microtubule disassembly. Consequently, hyperphosphorylated tau protein aggregates into insoluble NFTs, disrupting neuronal function and inducing apoptosis, resulting in neuronal death [4].

The amyloid precursor protein/ human presenilin 1 double-transgenic mouse model (APP/PS1 transgenic mice) is a valuable tool for studying AD. This model concurrently expresses the human APP and PS1 gene mutations [5]. The APP mutation enhances the β-secretase-mediated cleavage of APP, increasing Aβ precursor production, while the PS1 mutation alters γ-secretase activity, promoting Aβ production. This dual effect significantly increases Aβ accumulation in the brain, forming senile plaques and leading to neuroinflammation and neuronal damage, thereby recapitulating key pathological features of AD [6].

Transfer RNA (tRNA)-derived small RNAs (tsRNAs) are a newly identified class of small RNA molecules generated under various physiological and pathological conditions and are mediated by specific nucleases, such as Dicer and ANG [7]. Depending on their origin and mechanism of generation, tsRNAs can be categorized into tRNA-derived fragments (tRFs) and tRNA-derived stress-induced RNA (tiRNAs). Specifically, tRFs are further classified into tRF-1, tRF-2, tRF-3, and tRF-5 based on their cleavage patterns, while tiRNAs are classified into 3’-tiRNA and 5’-tiRNA. Each tRF or tiRNA subtype has different biological effects. tsRNAs play important roles in regulating gene expression and cellular functions through interactions with specific target genes, impacting post-transcriptional regulation and signal transduction pathways [8]. Recently, tsRNAs have been associated with various diseases, including cancer, neurological disorders, viral infections, and metabolic diseases [9]. However, the exact mechanisms by which tsRNAs influence AD remain largely unexplored.

The erythropoietin-producing hepatocellular (Eph) receptor family is the largest subgroup of receptor tyrosine kinases and plays essential role in various biological processes, including cell migration, neurodevelopment, angiogenesis, and tumor formation. Eph receptors are classified into two major types: EphA and EphB. Their ligands, known as ephrins, are membrane-bound proteins classified into ephrin-A and ephrin-B. The interaction between Eph receptors and ephrin ligands mediates their functions through bidirectional signaling [10]. Recently, the Eph receptor family has gained attention in the study of neurodegenerative diseases [11, 12]. Research has demonstrated that EphA4 and EphB2 are significant in AD. Activation of the EphA4 signaling pathway is linked to dysfunction of neuronal synapses, while downregulation of EphB2 is related to loss of synaptic plasticity [13–15]. However, few studies have investigated how tsRNAs regulate Eph signaling and influence AD pathology, prompting further exploration of tsRNAs as a regulatory factor in AD.

In our experiments, we identified a specific tsRNA, $tRF^{Ala\text{-}AGC\text{-}3\text{-}M8}$, derived from 5’-tRFs in the APP/PS1 transgenic mice expression profile. Following Aβ stimulation, the expression of $tRF^{Ala\text{-}AGC\text{-}3\text{-}M8}$ was significantly downregulated, leading to the upregulation of EphA7 within the Eph receptor family. EphA7 enhances hyperphosphorylation of the $ERK_{1/2}$ -p70S6K signaling pathway, exacerbating neuroinflammation and neuronal damage.

Methods

Animals and design

All animal precedures were approved by the Animal Experiment Ethics Committee of Southern Medical University. Eight-month-old male C57BL/6 mice and APP/PS1 transgenic mice(25 ± 3 g) were purchased from the Guangdong Experimental Animal Center. Animals were housed in groups of six per cage under a 12-hour light/dark cycle (lights on at 8:00 AM) with ad libitum access to food and water.

Cell culture and design

BV-2 (CL-0493) and HT22 (CL-0595) cells were provided by Wuhan Procell Life Science & Technology Co., Ltd. The cells were cultured in Dulbecco’s Modified Eagle Medium (DMEM), containing 10% fetal bovine serum (FBS) and 1% penicillin-streptomycin. When the cell growth density reached approximately 50%, BV-2 and HT22 cells were induced with $Aβ_{25\text{-}35}$ (HY-P0128, MedChemExpress, Shanghai, China) at concentrations of 0, 5, 10, 20, 30, and 40 μM. BV-2 cells were exposed for 24, 36, and 48 h, while HT22 cells were treated for 24 h.

RNA extraction, collection, and sample quality control

Total RNA was extracted from samples using RNAiso Plus (Takara Bio Cat. #9109) following the manufacturer’s protocol. The purity and concentration of total RNA samples were determined using a NanoDrop ND-1000 spectrophotometer (Thermo Fisher Scientific), with samples demonstrating an A_{260}/A_{280} ratio between 1.8-2.0 being retained for downstream analysis.

tsRNAs pretreatment and library construction

Before preparing libraries from total RNA samples, the following treatments were performed: 3’-deacylation (charged) to 3’-OH for 3’adaptor ligation, 3’-cP (2’,3’-cyclic phosphate) removal to 3’-OH for 3’ adaptor ligation, 5’-OH phosphorylation to 5’-P for 5’ adaptor ligation, and demethylation of m1A and m3C for efficient reverse transcription. RNA biotype selection for sequencing libraries was performed using an automated gel cutter. Library quality and absolute quantification were assessed using an Agilent BioAnalyzer 2100.

Sequencing data analysis

Raw sequencing data generated by Illumina NextSeq 500 underwent Illumina purity filtering and was used for subsequent analysis. Read sequences were trimmed (5' and 3' adaptor bases trimmed), allowing a single mismatch alignment with mature tRNA sequences, followed by alignment of unmatched read sequences with precursor tRNA sequences using Knot software. Alignment statistics (alignment rate, read length, and fragment sequence bias) guided the decision on the suitability of subsequent analyses. If applicable, expression profiling and differential expression analysis of tRF and tiRNA were performed. All visualizations were generated using R or Perl environments.

Prediction and bioinformatics analysis of tsRNAs-Target genes

Differentially expressed tsRNAs that met the criteria of fold change > 1.5 and p-value < 0.05 were selected from the sequencing dataset. Subsequently, quantitative reverse transcription polymerase chain reaction (qRT-PCR) was used to further screen and validate differentially expressed tsRNAs consistent with sequencing results, designating them as candidate tsRNAs(Ca-tRFs). The interaction seed sequences between tsRNAs and their target genes were predicted using TargetScan and miRanda. Significant relationships between Ca-tRFs and their respective target genes were visualized using Cytoscape (version 3.9.1). Gene Ontology (GO) and Kyoto Encyclopedia of Genes and Genomes (KEGG) pathway annotations were used for functional enrichment analysis of Ca-tRFs target genes to correlate tsRNAs with different biological functions. These analyses were performed using R (version 4.3.1), with a significance threshold set at p-value < 0.05.

Table 1 Primer sequence

Gene name	Primer sequence
U6	F: 5′-CTCGCTTCGGCAGCACATATACT-3′ R: 5′-GTCGTATCCAGTGCAGGGTCCGAGGT-3′ RT: 5′-AAAATATGGAACGCTTCACGAATTTG-3′
tRF$^{\text{Ala–AGC–3–M8}}$	F:5′-GGGGATGTAGCTCAGT-3′ R: 5′-GTGCAGGGTCCGAGGT-3′ RT: 5′-GTCGTATCCAGTGCAGGGTCCGAGGTATTCGCACTGGATACGACACTGAGC-3′
tRF$^{\text{Gly–TCC–1}}$	F: 5′-GCGTTGGTGGTATAGTGGTGAGCATAG-3′ R: 5′-GTGCAGGGTCCGAGGT-3′ RT: 5′-GTCGTATCCAGTGCAGGGTCCGAGGTATTCGCACTGGATACGACGCAGCTA-3′
tiRNA$^{\text{Gly–CCC–2}}$	F:5′-GCATTGGTAGTTCAATGGTAGAATTCTC-3′ R: 5′-GTGCAGGGTCCGAGGT-3′ RT: 5′-GTCGTATCCAGTGCAGGGTCCGAGGTATTCGCACTGGATACGACGAGGCGA-3′
β-actin	F: 5′-CACTGTCGAGTCGCGTCC-3′ R: 5′-TCATCCATGGCGAACTGGTG-3′
EphA7	F: 5′-AACCGGGAACAGTGTACGTC-3′ R: 5′-GGAGACTGCTGTCGCTTCAA-3′

Quantitative reverse transcription polymerase chain reaction (qRT-PCR)

Total RNA was extracted using RNAiso Plus reagent (Takara Bio Cat. #9109) following the manufacturer's protocal. RNA concentration and purity were evaluated using a NanoDrop ND-1000 spectrophotometer. Subsequently, total RNA was reverse transcribed into cDNA using the PerfectStart® Uni RT&qPCR Kit (Transgen AUQ-01). PCR amplification was performed using PerfectStart® Green qPCR SuperMix (Transgen AQ602-01). qRT-PCR analysis was performed using an Applied Biosystems 7500 Real-Time PCR System (Thermo Fisher Scientific, USA) following the recommended PCR premix conditions. To ensure the reliability and reproducibility of the experiment, each reaction was independently repeated three times. RNA expression was normalized to those of β-actin and tsRNAs expression levels were normalized to those of U6. The $2^{\Delta\Delta Ct}$ method was used to analyze the relative RNA expression. Primer sequences are showed in Table 1.

EphA7-siRNA and tRF$^{\text{Ala–AGC–3–M8}}$ -mimic transfection

EphA7-targeting siRNA (EphA7-siRNA) and non-specific control siRNA (NC-siRNA), as well as chemically synthesized double-stranded tRF$^{\text{Ala-AGC-3-M8}}$ mimic (tRF$^{\text{Ala-AGC-3-M8}}$ -mimic) and non-specific control mimics (NC-mimic), were purchased from RIBOBIO Biotechnology Co., Ltd., China. EphA7-siRNA or NC-siRNA, tRF$^{\text{Ala-AGC-3-M8}}$-mimic or NC-mimic were transfected using Lipofectamine 3000 (Invitrogen, USA) into BV-2 or HT22 cells according to the manufacturer's protocol, and the transfection process lasted for 24–36 h.

Dual-luciferase assay

After designing wild-type (WT) and mutant(MUT) EphA7 sequences, the sequences were cloned downstream of the Renilla luciferase gene (hRluc) in the pmiR-RB-Report™ plasmid vector. The WT plasmid vector with tRF$^{\text{Ala-AGC-3-M8}}$-mimic, WT plasmid vector with NC-mimic, MUT plasmid vector with tRF$^{\text{Ala-AGC-3-M8}}$-mimic, or MUT plasmid vector with NC-mimic was co-transfected into BV-2 cells. After 36 h, the cells were treated with cell lysis buffer. A suitable amount of lysis buffer (typically 100 – 200 μL) was added to each well, and the cells were gently pipetted to ensure complete lysis. Firefly luciferase substrate and Renilla luciferase substrate were prepared according to the manufacturer's instructions. 100 μL of cell lysate was added to the wells of the luciferase detection plate. Firefly luciferase substrate was added and mixed. The firefly luciferase signal was immediately measured using a luminometer. Renilla luciferase substrate was then added to the same lysate. Reading parameters were set according to the luminometer protocol, with firefly and Renilla luciferase signals read separately.

Western blotting (WB)

Lysates from tissues and cells were prepared using RIPA buffer with protease/phosphatase inhibitors. Proteins (10–30 μg) were separated on 7.5 – 10% SDS-PAGE gels (Thermo Fisher) and transferred to PVDF membranes (Merck Millipore). Membranes were blocked with 5% bovine serum albumin (BSA; Sigma-Aldrich, Cat. #A7906) (1 h, RT) and incubated overnight at 4 °C with primary antibodies (p-tau, EphA7, $ERK_{1/2}$, p-$ERK_{1/2}$, p70S6K, p-p70S6K, iNOS, β-actin, β-Tubulin; 1:1,000 – 1:10,000, Bioworld). After washing, membranes were incubated with HRP-conjugated secondary antibodies (1:1,000 – 1:10,000, Bioworld; 2 h, RT). Proteins were detected using ECL substrate (Pierce, Cat. #32106) and imaged with a ChemiDoc™ System (BioRad). Each experiment was repeated three times independently. Band intensities were quantified using Fiji ImageJ and normalized to β-actin/β-tubulin.

Immunofluorescence staining (IF)

Tissues were embedded, sectioned, and deparaffinized. Cells were washed, centrifuged, and resuspended in PBS. Samples were fixed with 4% paraformaldehyde (PFA) (20mins, RT), permeabilized with 0.1% Triton X-100 (10–15 min, RT), and washed 3x with PBS. Non-specific binding was blocked with 5% goat serum (NGS; Sigma-Aldrich, Cat.#G9023) (1 h, RT). Samples were incubated overnight at 4°C with primary antibodies (iNOS, NeuN, Iba-1, p-tau, EphA7; 1:100 – 1:500, abcam), washed 3x with PBS, and incubated with fluorescent secondary antibodies (AlexaFluor 555/488/647; 1:1000, abcam; 1 h, RT, protected from light). Nuclei were stained with DAPI (5–10 mins, RT), washed 2x with PBS, and imaged using Leica fluorescence microscope or Leica TCS SP8 confocal microscope.

Statistical analysis

The data were analyzed using R (Version 4.3.1) and GraphPad Prism (Version 9.5.1). For comparisons between two groups, two-tailed Student's t-test was used for parametric data. For comparisons between multiple groups, one-way analysis of variance was performed, followed by post-hoc tests (e.g., Tukey's HSD or Bonferroni correction) for parametric data. Statistical significance was set at $p < 0.05$.

Result

Downregulation of $tRF^{Ala\text{-}AGC\text{-}3\text{-}M8}$ expression in APP/PS1 transgenic mice cortex

We comprehensively analyzed the expression profile of tsRNAs in APP/PS1 transgenic mice cortex using tsRNA-Seq technology. Our results showed an increase in the proportion of 5'-tiRNA and tRF-5c with a decrease in the proportion of tRF-5a in APP/PS1 mice (**Fig. 1A**). We identified tsRNAs with significant differential expression based on fold change (cut-off value of 1.5) and p-value (only when there were replicates, cut-off value of 0.05). This analysis revealed 25 tsRNAs with significant differential expression in the APP/PS1 transgenic mice expression profile, including 13 upregulated and 12 downregulated tsRNAs, among which there were 12 types of 5'tsRNAs (**Fig. 1B and C**). The verification results for three 5'tsRNAs, including $tiRNA^{Gly\text{-}CCC\text{-}2}$ (upregulated, tiRNA-5, p-value = 0.0202), $tRF^{Ala\text{-}AGC\text{-}3\text{-}M8}$ (downregulated, tRF-5a, p-value = 0.0491), and $tRF^{Gly\text{-}TCC\text{-}1}$ (downregulated, tRF-5c, p-value = 0.0346), were consistent with the sequencing results (**Fig. 1D**).

$tRF^{Ala\text{-}AGC\text{-}3\text{-}M8}$ directly binds to the 3′ untranslated region (3′ UTR) region of EphA7

To further identify significant tsRNAs and their associated biological processes, we used bioinformatics tools. Leveraging the miRNA-like mechanism of tsRNAs, where their seed sequences (two to seven nucleotides at the 5' end) recognize target mRNAs, we predicted all mRNAs targeted by $tiRNA^{Gly\text{-}CCC\text{-}2}$, $tRF^{Ala\text{-}AGC\text{-}3\text{-}M8}$, and $tRF^{Gly\text{-}TCC\text{-}1}$. We then identified the top 150 target genes for each tsRNA based on higher structure score, lower free energy, and context plus score and presented these findings through a tsRNA-Target genes interaction network (**Fig. 2A**). Notably, EphA7 was the only member of the Eph family interacting with $tiRNA^{Gly\text{-}CCC\text{-}2}$ (structure score: 152, energy score: 12.98, context plus score: -1.74), $tRF^{Ala\text{-}AGC\text{-}3\text{-}M8}$ (structure score: 146, energy score: 16.75, context plus score: -4.27), and $tRF^{Gly\text{-}TCC\text{-}1}$ (structure score: 144, energy score: -2.86, context plus score: -5.29). We further illustrated the binding patterns of these three tsRNAs with the 3' UTR region of EphA7 based on their binding sequences. The results indicated that $tRF^{Ala\text{-}AGC\text{-}3\text{-}M8}$ binds to the 3' UTR region of EphA7 with an 8mer-1a binding pattern, a highly accurate matching mode (**Fig. 2B**).

To further verify the binding with the 3' UTR region of EphA7, we designed WT (5'ccTGAAAAACATCCa3') and mutant (5'ccACTAAATGTAGGGa3') 3' UTR sequences of EphA7 and cloned these sequences into plasmid vectors to create WT and MUT pmiR-RB-Report™ vectors. We transfected these WT or MUT plasmids (Group: EphA7-WT, EphA7-MUT), alongside $tRF^{Ala\text{-}AGC\text{-}3\text{-}M8}$-mimic or NC-mimic (Group: AGC-3-M8,

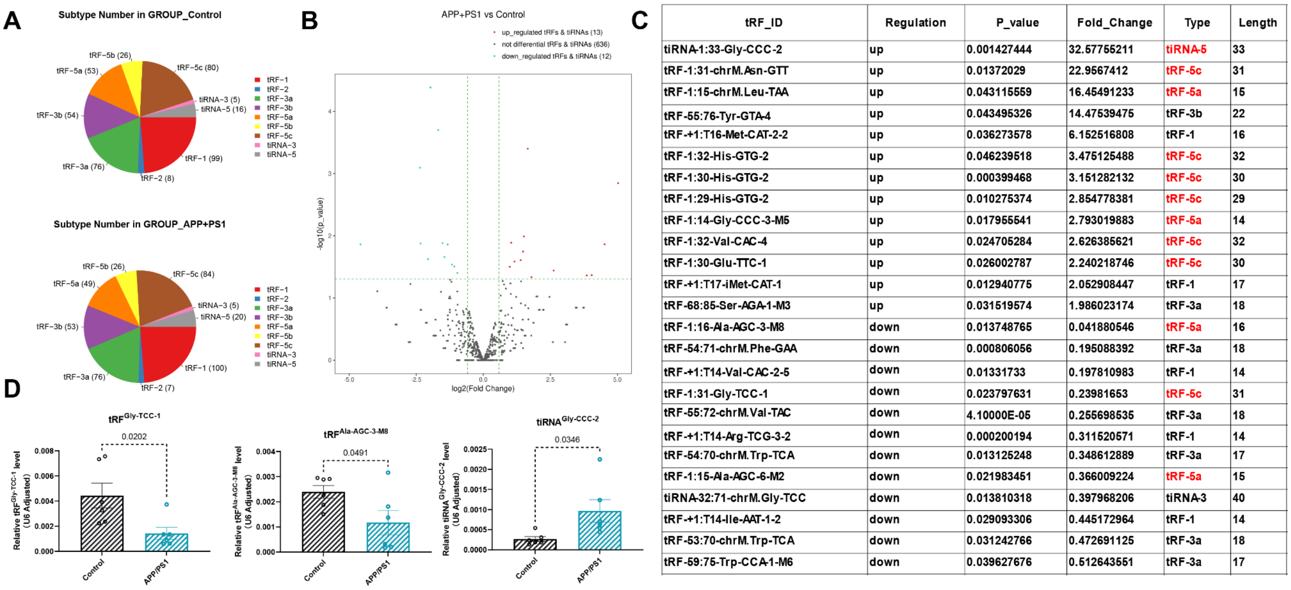

tRF_ID	Regulation	P_value	Fold_Change	Type	Length
tiRNA-1:33-Gly-CCC-2	up	0.001427444	32.57755211	tiRNA-5	33
tRF-1:31-chrM.Asn-GTT	up	0.01372029	22.9567412	tRF-5c	31
tRF-1:15-chrM.Leu-TAA	up	0.043115559	16.45491233	tRF-5a	15
tRF-55:76-Tyr-GTA-4	up	0.043495326	14.47539475	tRF-3b	22
tRF-+1:T16-Met-CAT-2-2	up	0.036273578	6.152516808	tRF-1	16
tRF-1:32-His-GTG-2	up	0.046239518	3.475125488	tRF-5c	32
tRF-1:30-His-GTG-2	up	0.000399468	3.151282132	tRF-5c	30
tRF-1:29-His-GTG-2	up	0.010275374	2.854778381	tRF-5c	29
tRF-1:14-Gly-CCC-3-M5	up	0.017955541	2.793019883	tRF-5a	14
tRF-1:32-Val-CAC-4	up	0.024705284	2.626385621	tRF-5c	32
tRF-1:30-Glu-TTC-1	up	0.026002787	2.240218746	tRF-5c	30
tRF-+1:T17-iMet-CAT-1	up	0.012940775	2.052908447	tRF-1	17
tRF-68:85-Ser-AGA-1-M3	up	0.031519574	1.986023174	tRF-3a	18
tRF-1:16-Ala-AGC-3-M8	down	0.013748765	0.041880546	tRF-5a	16
tRF-54:71-chrM.Phe-GAA	down	0.000806056	0.195088392	tRF-3a	18
tRF-+1:T14-Val-CAC-2-5	down	0.01331733	0.197810983	tRF-1	14
tRF-1:31-Gly-TCC-1	down	0.023797631	0.23981653	tRF-5c	31
tRF-55:72-chrM.Val-TAC	down	4.10000E-05	0.255698535	tRF-3a	18
tRF-+1:T14-Arg-TCG-3-2	down	0.000200194	0.311520571	tRF-1	14
tRF-54:70-chrM.Trp-TCA	down	0.013125248	0.348612889	tRF-3a	17
tRF-1:15-Ala-AGC-6-M2	down	0.021983451	0.366009224	tRF-5a	15
tiRNA-32:71-chrM.Gly-TCC	down	0.013810318	0.397968206	tiRNA-3	40
tRF-+1:T14-Ile-AAT-1-2	down	0.029093306	0.445172964	tRF-1	14
tRF-53:70-chrM.Trp-TCA	down	0.031242766	0.472691125	tRF-3a	18
tRF-59:75-Trp-CCA-1-M6	down	0.039627676	0.512643551	tRF-3a	17

Fig. 1 Comprehensive tsRNA expression profile in APP/PS1 transgenic mice analyzed using tsRNA-Seq. **(A)** Distribution of tsRNA subtypes, showing an increased proportion of 5′-tiRNA and tRF-5c and a decreased proportion of tRF-5a in APP/PS1 transgenic mice cortex compared to controls (Control and APP/PS1: $n = 3$, biologically independent samples). **(B)** Volcano plot of tsRNA expression, highlighting 25 tsRNAs with significant differential expression (13 upregulated and 12 downregulated). **(C)** Specific information of differentially expressed tsRNAs, with 5′ tsRNAs marked in red. **(D)** qRT-PCR analysis of 5′ tsRNAs. $tiRNA^{Gly-CCC-2}$, $tRF^{Ala-AGC-3-M8}$, and $tRF^{Gly-TCC-1}$ showed consistent results with the sequencing data ($n = 6$, biologically independent samples). Statistical significance was assessed using Student's t-test **(D)** (p-value < 0.05; p values are indicated). All data are presented as means ± SEM. Each data point represents the average of 3 technical replicates

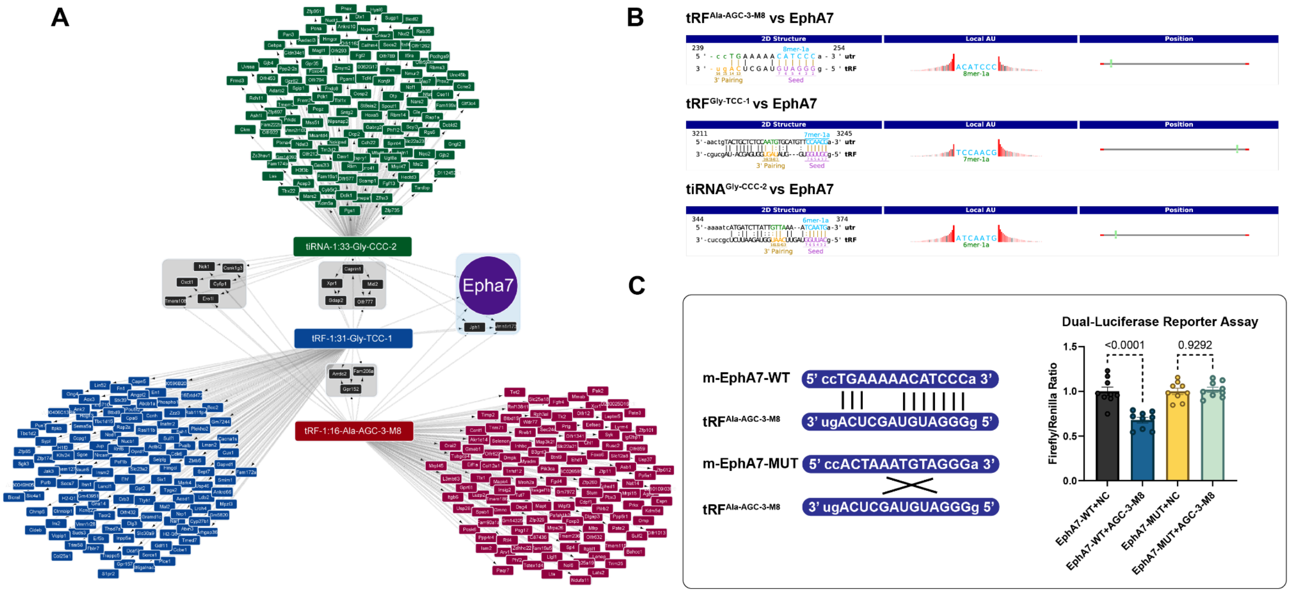

Fig. 2 Identification and validation of tsRNA-Target genes interactions and binding patterns. **(A)** The tsRNA-Target genes interaction network identifies EphA7 as a common target. **(B)** $tRF^{Ala-AGC-3-M8}$ binds to the EphA7 3′ UTR through an 8mer-1a pattern. 2D structure: The specific location of the binding site in the 3′ UTR (mRNA) or throughout a particular sequence. Local AU: AU weight distribution diagram around the seed sites, which influences site accessibility. The evaluation function slightly varies depending on the type of seed. The red bar indicates the position is A, with a higher number being more favorable. Position: The relative location of the site on the UTR, with proximity to the edges being more optimal. **(C)** Dual-Luciferase Reporter Assay results show that $tRF^{Ala-AGC-3-M8}$-mimic significantly decreases firefly luciferase activity (adjusted by renilla luciferase, normalized to NC mimic) in the EphA7-WT group ($n = 9$, biologically independent samples). Statistical significance was assessed using Student's t-test (p-value < 0.05; P values are indicated). All data are expressed as means ± SEM. Each data point represents the average of 3 technical replicates

NC) into BV-2 cells. After 36 hours, we measured luciferase activity (normalized to firefly luciferase). The results showed that tRF$^{Ala\text{-}AGC\text{-}3\text{-}M8}$-mimic significantly decreased firefly luciferase activity in the WT group compared to the NC-mimic group (p-value<0.0001), while no significant difference was observed in the MUT group. This result convincingly confirmed that tRF$^{Ala\text{-}AGC\text{-}3\text{-}M8}$ binds to the EphA7 3' UTR region and inhibits EphA7 translation (Fig. 2C).

Enrichment analysis of tRF$^{Ala\text{-}AGC\text{-}3\text{-}M8}$ target genes

To understand the role and relationship of the predicted tRF$^{Ala\text{-}AGC\text{-}3\text{-}M8}$ target genes in signaling pathways, we performed KEGG and GO enrichment analyses. KEGG enrichment analysis reveals that the axon guidance pathway had the highest score among the signaling pathways associated with tRF$^{Ala\text{-}AGC\text{-}3\text{-}M8}$ target genes (**Fig.** 3**A**). We further illustrated the gene codes involved in the axon guidance pathway using a Pathway–Gene network diagram (**Fig.** 3**B**), which indicates the involvement of EphA7. GO enrichment analysis demonstrates that the synapse organization pathway had the highest score among the biological processes associated with tRF$^{Ala\text{-}AGC\text{-}3\text{-}M8}$ target genes (**Fig.** 3**C**). We also constructed Biological Process-Gene waterfall plot (**Fig.** 3**D**) to elaborate the biological processes involving EphA7, which highlights synapse organization, regulation of synapse organization and activity, post-synapse organization, and cell junction assembly. These results suggest that the target genes of significantly differentially expressed tsRNAs in the APP/PS1 transgenic mice expression profiles are closely related to axon guidance and synapse organization, with EphA7 being significantly involved in both processes.

Upregulation of EphA7 was detected in microglial aggregates and neurons localized to the dentate gyrus (DG)

To investigate the characteristic expression changes of EphA7 in APP/PS1 transgenic mice, we analyzed the brain slices. The results showed scattered Iba-1$^+$/EphA7$^+$ cell clusters in the cortex (**Fig.** 4**A**), with significantly increased fluorescence area and intensity compared to the control group (p-value<0.0001). These cells often appeared as irregular circular shapes surrounding cell with weak NeuN$^+$ fluorescence signals (**Fig.** 4**C**). Additionally, in both the head (**Fig.** 5**A**) and tail (**Fig.** 5**E**) hippocampus of APP/PS1 transgenic mice, NeuN$^+$/EphA7$^+$ cells with higher EphA7 fluorescence signals (p-value<0.0001) were distributed throughout the DG of the hippocampus, whereas these cells were not observed in Cornu Ammonis (CA) region.

Downregulation of tRF$^{Ala\text{-}AGC\text{-}3\text{-}M8}$ and upregulation of EphA7 after A$\beta_{25\text{-}35}$ induction

The downregulation of tRF$^{Ala\text{-}AGC\text{-}3\text{-}M8}$ (**Fig.** 1**D**) and upregulation of Epha7 (**Fig.** 4 and **Fig.** 5) have been observed in the APP/PS1 transgenic mice. To further explore these changes, we conducted in vitro experiments using BV-2 and HT22 cells.

In the HT22 cells, compared to the control group (A$\beta_{25\text{-}35}$, 0 μM), all treatment groups (A$\beta_{25\text{-}35}$, 5 μM, 10 μM, 20 μM, 30 μM, and 40 μM) exhibited irregular shrinkage of neuronal cell bodies and shortened

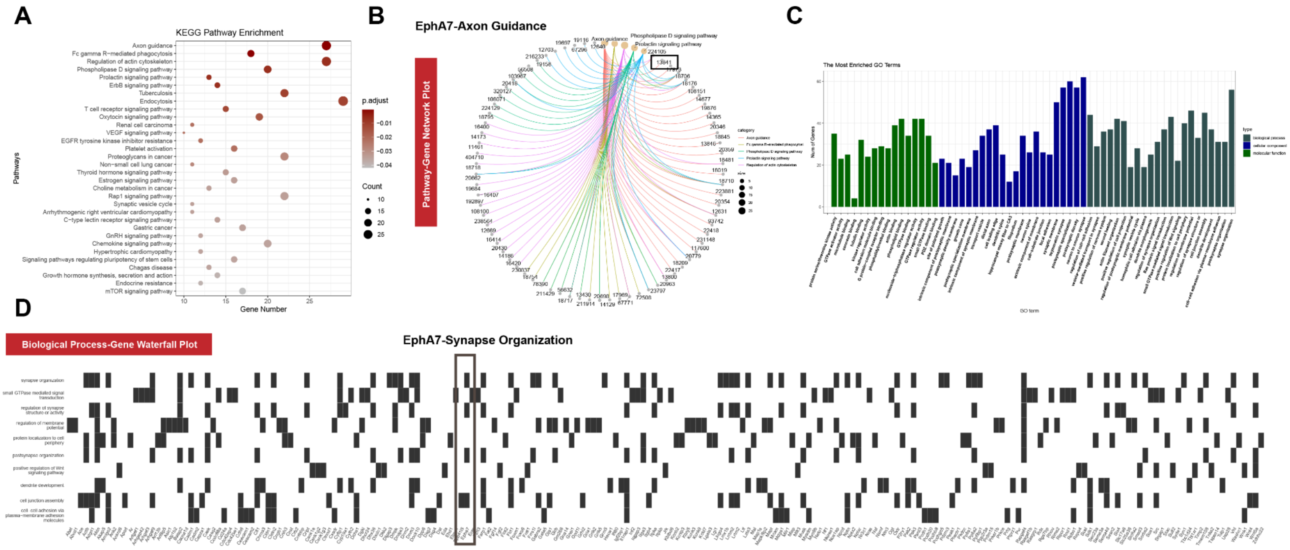

Fig. 3 KEGG and GO enrichment analyses of tRFAla–AGC–3–M8 target genes. (A) KEGG analysis identified the axon guidance pathway as the most significant for the predicted target genes. (B) Pathway-Gene network diagram showing that EphA7 (Universal Protein Resource ID: 13041, labeled with a black box) is involved in the axon guidance pathway. (C) GO analysis revealed synapse organization as the key biological process. (D) Biological Process-Gene Waterfall plot illustrating EphA7's role in synapse-related activities (labeled with a black box)

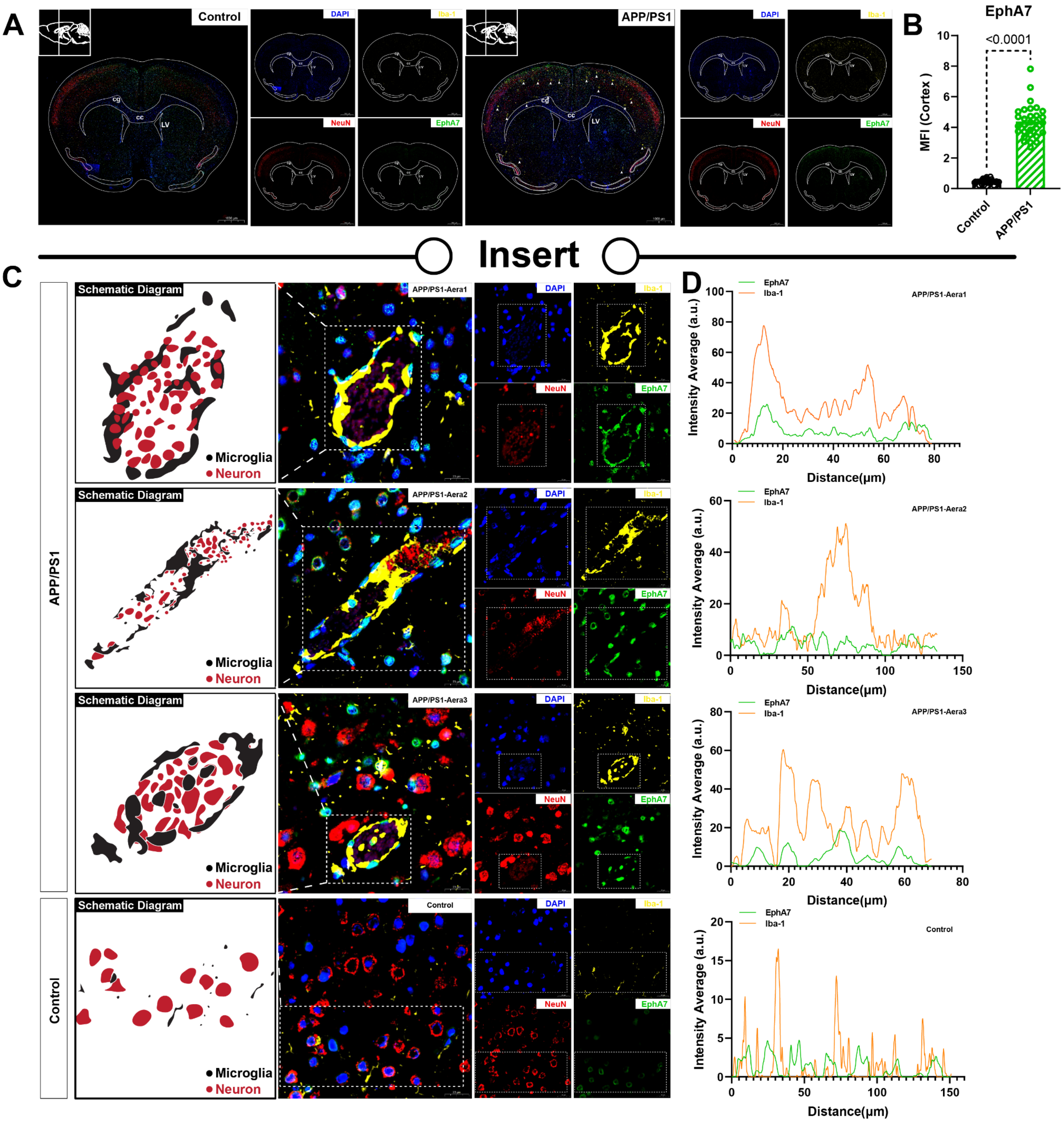

Fig. 4 EphA7 expression in the cortex of APP/PS1 transgenic mice. **(A)** Brain slices from the APP/PS1 transgenic mice show Iba-1^+ cell clusters (marked with white arrows) in the cortex, with higher expression of EphA7. Scale bar: 1000 μm. **(B)** Mean fluorescence intensity analysis of EphA7 expression in the cortex ($n = 6$, biologically independent samples). **(C)** Zoomed-in immunofluorescence image of the cortex. Scale bar: 20 μm. The fluorescence signal was manually traced to enhance visualization in schematic diagram (black: microglia; red: neuron). **(D)** Immunofluorescence analysis of Iba-1 (orange) and EphA7 (green) localization. Statistical significance was assessed using Student's t-test (P values are indicated). All data are presented as means ± SEM. Each data point represents the experimental measure

processes, with damage increasing at higher $A\beta_{25\text{-}35}$ stimulation concentrations. After 24 h, the 30 μM and 40 μM concentration groups showed nearly complete loss of intact cell structures. For $tRF^{Ala\text{-}AGC\text{-}3\text{-}M8}$, the 5 μM (p-value<0.0001), 10 μM (p-value<0.0001), 20 μM (p-value<0.0001), 30μM (p-value = 0.0012) groups demonstrated downregulation of $tRF^{Ala\text{-}AGC\text{-}3\text{-}M8}$ (**Fig.** 6**A**).

In the BV-2 cells, cell morphology changes were assessed at induction of $A\beta_{25\text{-}35}$ for 24, 36 and 48 h to modify the difference response of BV-2 cell simulated

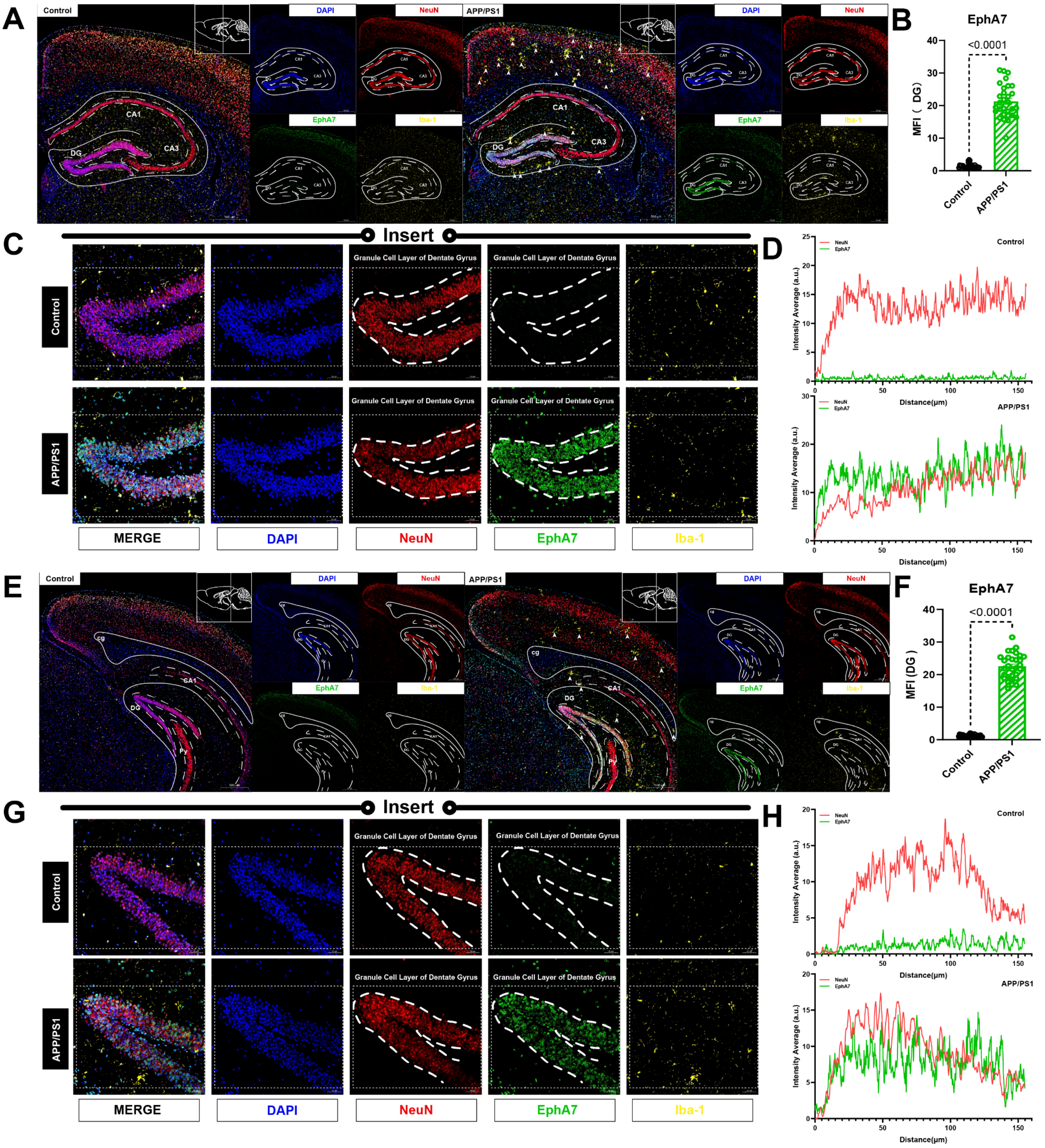

Fig. 5 EphA7 expression in the hippocampus of APP/PS1 transgenic mice. **(A, E)** Immunofluorescence image show significant EphA7 overexpression in the hippocampus of DG; Scale bar: 500μm. **(B, F)** Mean fluorescence intensity of EphA7 in the dentate gyrus ($n = 6$, biologically independent samples). **(C, G)** Zoomed-in immunofluorescence image of the dentate gyrus; Scale bar: 50 μm. **(D, H)** Immunofluorescence analysis of NeuN (red) and EphA7 (green) localization. Statistical significance was assessed using Student's t-test (B and F) (p values are indicated). All data are presented as means ± SEM. Each data point represents the experimental measure

by A$\beta_{25\text{-}35}$. After 24 h of A$\beta_{25\text{-}35}$ induction, all treatment groups showed slight aggregation; however, the morphological changes were not obvious. At this point, qRT-PCR analysis indicated that tRF$^{\text{Ala-AGC-3-M8}}$ expression levels were significantly higher in the treatment groups compared to the control group (fold changes > 5, peaking at > 40-fold).tRF$^{\text{Ala-AGC-3-M8}}$ expression levels exhibited a concentration-dependent increase though the

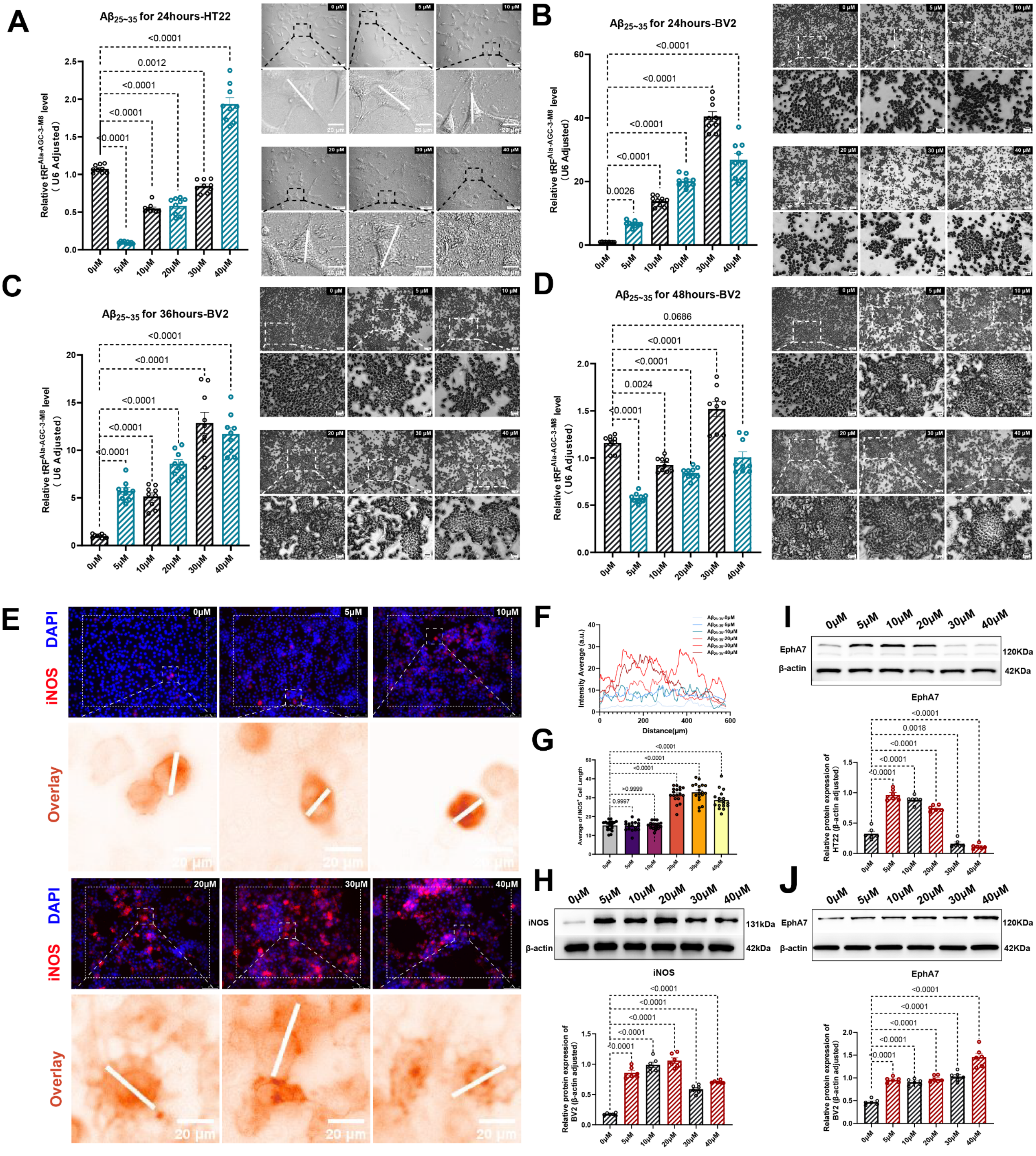

Fig. 6 Characterization of tRFAla–AGC–3–M8 and EphA7 expression in in vitro models of AD. (A–D) qRT-PCR analysis of tRFAla–AGC–3–M8 expression in HT22 cells (after 24 h induction with Aβ25–35) and BV-2 cells (after 24, 36, or 48 h induction with Aβ25–35; *n* = 6, biologically independent samples); Scale bar: 75μm (overview), 20μm (insert). (E, F) Immunofluorescence analysis of iNOS localization in BV-2 cells after 48 h induction with Aβ25–35. The distance–intensity average curve demonstrates the characteristic expression profile of iNOS in BV-2 cells treated with Aβ25–35 (*n* = 6, biologically independent samples). **(G)** Measurement of cell length in iNOS + BV-2 cells (*n* = 6, biologically independent samples); Scale bar: 75μm (overview), 20 μm (insert). (H–J) Western blot analysis of iNOS and EphA7 expression in BV-2 and HT-22 cells following treatment with Aβ25–35 for 24 or 48 h (*n* = 6, biologically independent samples); Statistical significance was assessed using one-way ANOVA (P values are indicated). All Data are presented as means ± SEM. Each data point represents the average of 3 technical replicates

40 μM group was lower compared to the 30 μM group (**Fig. 6B**). After 36 h of induction, cells in the treatment group showed increased aggregation and cluster areas compared to 24 h of $A\beta_{25\text{-}35}$ stimulation. At this stage, the cell morphology became irregular and star-shaped. qRT-PCR detection showed that $tRF^{Ala\text{-}AGC\text{-}3\text{-}M8}$ expression levels were significantly higher in the treatment groups compared to the control group, but the fold changes decreased, with only the 30 μM and 40 μM groups showing fold changes > 10, while other concentration groups exhibited fold changes < 10 (**Fig. 6C**). After 48 h of induction, cells of the treatment group showed significant morphological changes, tending toward M1-type polarization (enlarged cell bodies and radiating pseudopodia). Morphological changes were more predominantly toward the center of the clusters (**Fig. 6D**). Immunofluorescence analysis of iNOS expression showed that $iNOS^+$ cells were clustered, with higher $iNOS^+$ fluorescence intensity closer to the center (**Fig. 6E** and **F**). Cells in the 20 μM treatment group were mostly star-shaped, while cells in the < 20 μM treatment groups were merely round (**Fig. 6E** and **G**). Western blot analysis of iNOS protein expression levels after 48 h of $A\beta_{25\text{-}35}$ induction showed that all treatment groups exhibited higher levels than the control group (**Fig. 6H**). Both HT22 ($A\beta_{25\text{-}35}$, 5 μM, 10 μM, 20 μM) and BV-2 cells ($A\beta_{25\text{-}35}$, 5 μM, 10 μM, 20 μM, 30μM, 40μM) expressed high EphA7 after $A\beta_{25\text{-}35}$ induction for 24 h (HT22) or 48 h (BV-2) (**Fig. 6I** and **J**).

Activation of $ERK_{1/2}$-p70S6K signaling pathway after Aβ stimulation

Since the specific signaling pathways of EphA7 in AD are not well defined, we investigated potential signaling pathways involving EphA7 in APP/PS1 transgenic mice. WB analysis showed that in APP/PS1 transgenic mice, the phosphorylation of $ERK_{1/2}$ ($p\text{-value} < 0.0001$) and p70S6K (T421/S424) ($p\text{-value} < 0.0001$) were significantly increased (**Fig. 7A**). Parallel in vitro experimentsindicated that in BV-2 cells, the phosphorylation levels of $ERK_{1/2}$ ($p\text{-value} < 0.0001$) and p70S6K (T421/S424) ($p\text{-value} < 0.0001$) were significantly increased in the 5 μM and 20 μM $A\beta_{25\text{-}35}$ treatment groups ($p\text{-value} < 0.0001$) (**Fig. 7B**). Similarly, in HT22 cells, phosphorylation levels of $ERK_{1/2}$ ($p\text{-value} < 0.0001$) and p70S6K (T421/S424) (p-value$p < 0.0001$) were significantly elevated in the 10 μM and 20 μM $A\beta_{25\text{-}35}$ treatment groups (**Fig. 7C**).

Inhibition of EphA7 or upregulation of $tRF^{Ala\text{-}AGC\text{-}3\text{-}M8}$ suppresses $ERK_{1/2}$ and p70S6K phosphorylation, reducing M1-type polarization and Tau phosphorylation

The $ERK_{1/2}$-p70S6K pathway is activated after $A\beta_{25\text{-}35}$ stimulation (**Fig. 7**). To explore whether $tRF^{Ala\text{-}AGC\text{-}3\text{-}M8}$ affects the $ERK_{1/2}$-p70S6K signaling pathway, we transfected the $tRF^{Ala\text{-}AGC\text{-}3\text{-}M8}$-mimic (Group: ON-AGC-3-M8) and NC-mimic (Group: Control-mimic-NC; AD-mimic-NC) into BV-2 cells. After 24 h, qRT-PCR analysis was performed to measure the expression levels of $tRF^{Ala\text{-}AGC\text{-}3\text{-}M8}$ and EphA7. The results showed that $tRF^{Ala\text{-}AGC\text{-}3\text{-}M8}$ was significantly increased in BV-2 cells after transfection (fold change > 5, $p\text{-value} < 0.0001$), whereas EphA7 did not show any significant changes ($p\text{-value} = 0.5695$). (**Fig. 8A**). Subsequently, 48 h of $A\beta_{25\text{-}35}$ stimulation was conducted in transfected cells, total protein expression levels were measured by WB. The results demonstrated that, in BV-2 cells transfected with NC-mimic, EphA7 expression levels were increased with hyperphosphorylation levels of $ERK_{1/2}$ ($p\text{-value}<0.0001$)and p70S6K ($p\text{-value}<0.0001$), while cells transfected with $tRF^{Ala\text{-}AGC\text{-}3\text{-}M8}$-mimic showed decreased EphA7 ($p\text{-value}<0.0001$) (**Fig. 8B** and **D**) expression and significantly reduced phosphorylation levels of $ERK_{1/2}$ ($p\text{-value}<0.0001$) and p70S6K ($p\text{-value}<0.0001$) (**Fig. 8C** and **D**). Accordingly, cells transfected with the $tRF^{Ala\text{-}AGC\text{-}3\text{-}M8}$-mimic exhibited reduced aggregation, increased cell density, and a more normal morphology (**Fig.** 8E), along with a significant decrease in average iNOS fluorescence expression ($p\text{-value}<0.0001$) (**Fig. 8F** and **G**) and the distribution of $iNOS^+$ BV-2 cells is relatively uniform (**Fig. 8F** and **H**). To verify that whether the inhibition of the $ERK_{1/2}$-p70S6K pathway by $tRF^{Ala\text{-}AGC\text{-}3\text{-}M8}$ was achieved through suppressing EphA7 expression, we performed EphA7-siRNA (Group: Si-EphA7) or NC-siRNA (Group: Control-NC; AD-NC) transfections in BV-2 cells. After 24 h of transfection and following 48 h of $A\beta_{25\text{-}35}$ stimulation, total protein expression levels were measured by WB. The result shows that the EphA7-siRNA significantly downregulates the expression of EphA7 mRNA ($p\text{-value}<0.0001$) while exerting no discernible impact on the levels of $tRF^{Ala\text{-}AGC\text{-}3\text{-}M8}$ ($p\text{-value} = 0.6415$) (**Fig. 8I**). Additionally, EphA7-siRNA transfected BV-2 cell were consistent with those of the $tRF^{Ala\text{-}AGC\text{-}3\text{-}M8}$-mimic treatment, with normalization of cell morphology, reduced $iNOS^+$-BV2 cell aggregation (**Fig. 8M**), decreased EphA7 ($p\text{-value}<0.0001$)expression (**Fig. 8J** and **L**), significantly reduced phosphorylation of $ERK_{1/2}$ ($p\text{-value}<0.0028$)and p70S6K ($p\text{-value}<0.0001$) (**Fig. 8K** and **L**), and decreased iNOS expression (**Fig. 8N, O** and **P**).

Based on the BV-2 cell validation results, we then transfected HT22 cells with $tRF^{Ala\text{-}AGC\text{-}3\text{-}M8}$-mimic (Group: ON-AGC-3-M8), NC-mimic (Group: Control-mimic-NC; AD-mimic-NC), EphA7-siRNA (Group: Si-EphA7), or NC-siRNA (Group: Control-NC; AD-NC). After 24 h of transfection, qRT-PCR analysis was performed to measure the transcript levels of $tRF^{Ala\text{-}AGC\text{-}3\text{-}M8}$ and EphA7. The results showed that $tRF^{Ala\text{-}AGC\text{-}3\text{-}M8}$-mimic only increased $tRF^{Ala\text{-}AGC\text{-}3\text{-}M8}$ levels ($p\text{-value} <0.0001$)without affecting Epha7 transcription ($p\text{-value} = 0.6555$) and

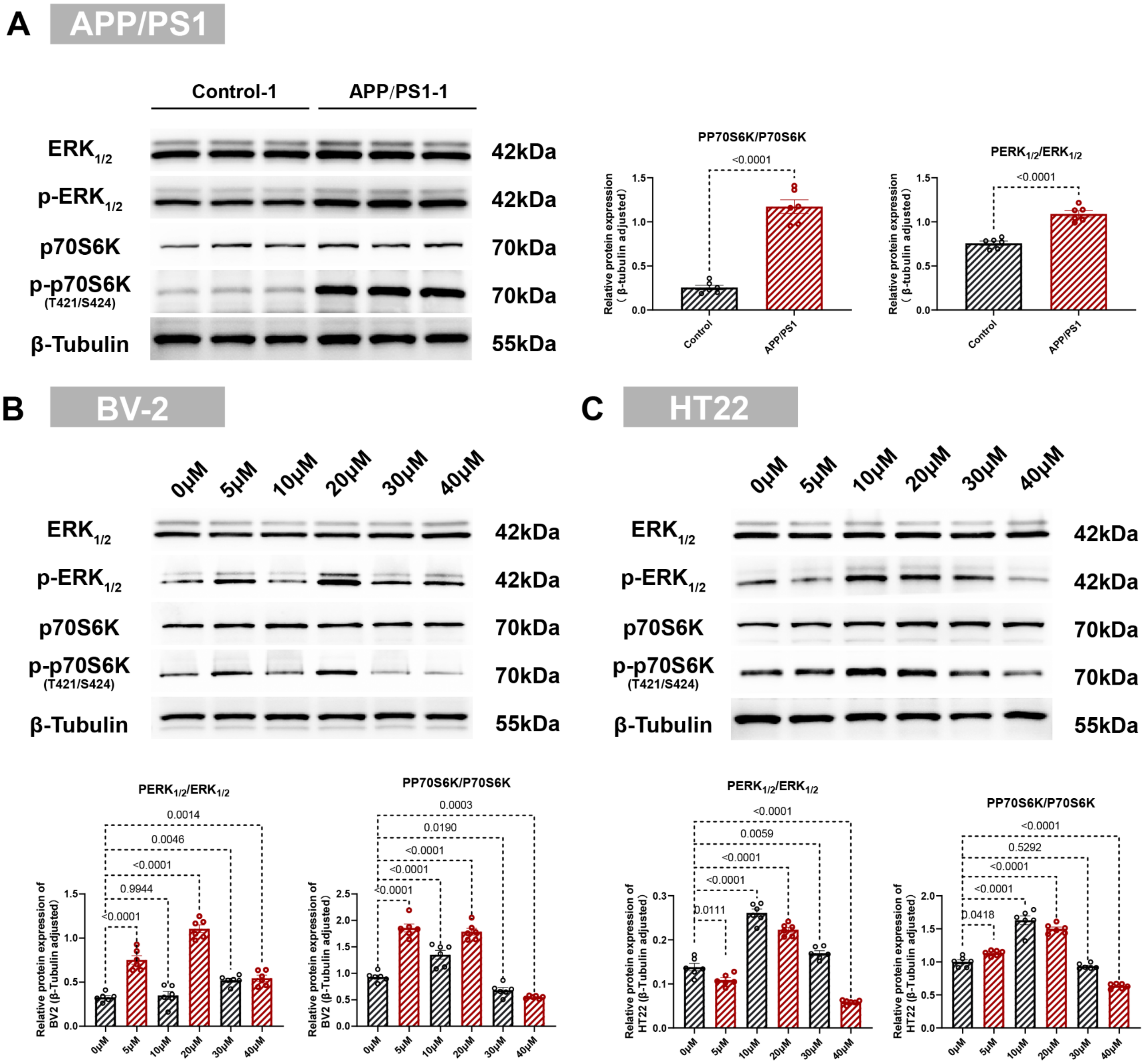

Fig. 7 Western blot analysis of $ERK_{1/2}$ and p70S6K phosphorylation in vivo and vitro model of AD. **(A)** Western blot analysis revealed a significant increase in the phosphorylation of $ERK_{1/2}$ and p70S6K (T421/S424) in the APP/PS1 transgenic mice group compared to the control group (*n* = 6, biologically independent samples). **(B)** Phosphorylation of $ERK_{1/2}$ and p70S6K (T421/S424) was increased in BV-2 cells treated with varying concentrations of $A\beta_{25-35}$ (5 μM and 20 μM), *n*=6 samples/group. **(C)** HT22 cells treated with $A\beta_{25-35}$ at concentrations of 10 μM and 20 μM exhibited elevated phosphorylation of $ERK_{1/2}$ and p70S6K (T421/S424) (*n* = 6, biologically independent samples). Statistical significance was assessed using Student's test (A) and one-way ANOVA (B and C) (P values are indicated). All Data are presented as means ± SEM. Each data point represents the average of 3 technical replicates

the EphA7-siRNA downregulates the transcription level of Epha7 (p-value<0.0001) without impact on the levels of $tRF^{Ala\text{-}AGC\text{-}3\text{-}M8}$ (p-value = 0.3536) (**Fig. 9A**), which is consistent with the results in BV-2 cells. Subsequently, treatment groups were stimulated with 20μM $A\beta_{25-35}$ for 24 h. Total protein expression levels were measured by WB. The results showed that EphA7 expression (AD-mimic-NC: p-value<0.0001; AD-NC: p-value<0.0001) was significantly higher in the AD-mimic-NC and AD-NC groups than in the control group, with significantly increased phosphorylation of $ERK_{1/2}$ (AD-mimic-NC: p-value<0.0001; AD-NC: p-value<0.0001) and p70S6K (AD-mimic-NC: p-value<0.0001; AD-NC: p-value<0.0001) (**Fig. 9B and C**). HT22 cell morphology were changed to varying degrees, mostly linearly, with clustering distances between neuronal cell nuclei (**Fig. 9D**) accompanied by significantly increased tau protein phosphorylation (**Fig. 9E and F**). Conversely, the ON-AGC-3-M8 and Si-EphA7 groups showed decreased EphA7 expression levels, reduced phosphorylation of

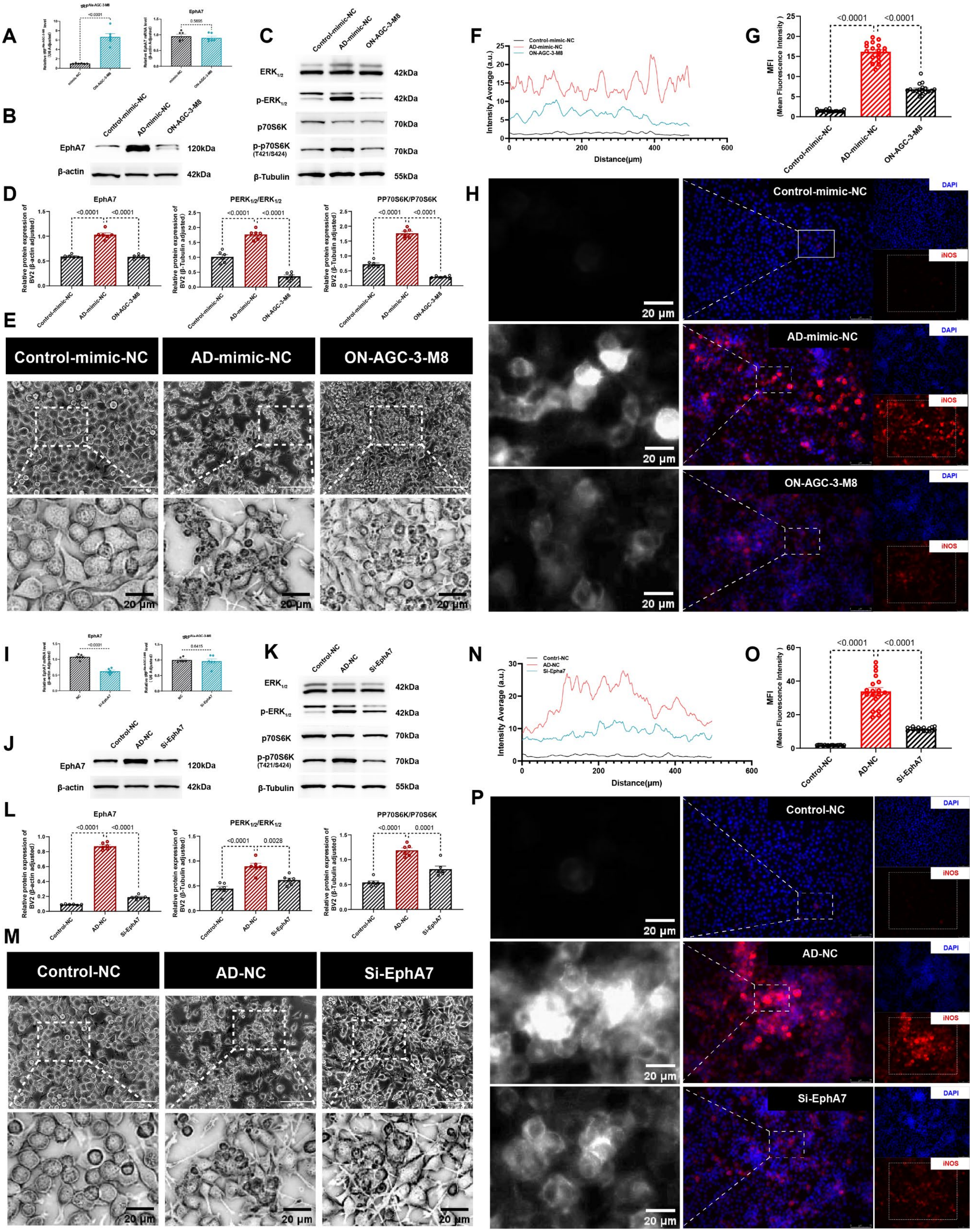

Fig. 8 (See legend on next page.)

(See figure on previous page.)

Fig. 8 Effects of tRF$^{Ala-AGC-3-M8}$ on ERK$_{1/2}$-p70S6K pathway in BV-2 cells. **(A, I)** qRT-PCR analysis of tRF$^{Ala-AGC-3-M8}$ and EphA7 in BV-2 cells after transfection with tRF$^{Ala-AGC-3-M8}$-mimic or EphA7-siRNA (n = 6, biologically independent samples). **(B-D, J-L)** Western blot analysis of EphA7 and phosphorylation of ERK$_{1/2}$ and p70S6K (T421/S424) in BV-2 cells (n = 6, biologically independent samples). **(E, M)** Representative light microscopy images of BV-2 cells morphological features; Scale bar: 75μm (overview), 20μm (insert). **(F-H, N-P)** Immunofluorescence localization an mean fluorescence intensity of iNOS in BV-2 cells (*n* = 6, biologically independent samples); Scale bar: 75μm (overview), 20μm (insert); Statistical significance was assessed using Student's test (A and I) and one-way ANOVA (D, L, G and O) (P values are indicated). All data are presented as the means ± SEM. Each data point represents the average of 3 technical replicates

ERK$_{1/2}$ (ON-AGC-3-M8: p-value<0.0001;Si-EphA7: p-value<0.0001) and p70S6K (ON-AGC-3-M8: p-value<0.0001; Si-EphA7: p-value<0.0001) (**Fig. 9B and C**), more directional neuron extension (**Fig. 9D**), and significantly lower tau protein phosphorylation (ON-AGC-3-M8: p-value<0.0001; Si-EphA7: p-value<0.0001) (**Fig. 9E and F**).

Discussion

AD is the most prevalent form of dementia among older adults. Although its etiology is not completely understood, it is generally believed to involve a combination of genetic, environmental, and lifestyle factors [16]. Current diagnostic methods rely on cognitive assessments, neuropsychological tests, neuroimaging techniques (such as magnetic resonance imaging and positron emission tomography), and cerebrospinal fluid analysis [17]. To date, there is no effective cure for AD; existing treatments only alleviate symptoms and improve quality of life. Therefore, developing and validating novel biomarkers, exploring novel drug targets, and formulating effective therapeutic strategies are critical for early and accurate diagnosis and treatment. Over the years, tsRNAs have garnered significant attention as emerging non-coding RNAs because of their high stability and specificity. tsRNAs play crucial roles in various biological processes, including gene regulation, cellular stress responses, and disease development [9]. Our study is the first to identify that tRF$^{Ala-AGC-3-M8}$ is significantly reduced in case of Aβ deposition in patients with AD. This reduction was negatively correlated with the expression of the target gene EphA7. EphA7 upregulation activates the ERK$_{1/2}$-p70S6K phosphorylation pathway, which promotes microglial M1-type polarization and enhances tau protein phosphorylation in neurons, leading to neuronal damage.

tRF and tiRNA from 5'end of tRNAs may be crucial in the pathology of AD. Current evidence suggests that tsRNAs from different sources have distinct biological functions [18], with 5'tRNAs playing vital roles in immunity, hematopoiesis, and intercellular communication [19]. In the context of AD, where neuroinflammation and dysregulated gene expression are hallmark features, the exploration of specific 5'tRNAs may uncover novel regulatory mechanisms underlying disease progression. In our study, we focused on identifying and characterizing 5'tRNAs with potential roles in AD pathogenesis. Through a combination of sequencing analysis and in vivo validation, we identified three key 5'tRNAs tiRNA-$^{Gly-CCC-2}$, tRF$^{Ala-AGC-3-M8}$, and tRF$^{Gly-TCC-1}$ as major regulatory molecules. Notably, our statistical results suggest that tRF$^{Ala-AGC-3-M8}$ interacts with EphA7 through an 8mer-1a binding pattern, indicating a perfect match between tRF$^{Ala-AGC-3-M8}$ and nucleotides 2 – 8 in the 3' UTR of EphA7, with A at position one, suggesting a novel mechanism by which tsRNAs may modulate gene expression in AD.

We confirmed the differential expression of EphA7 in AD and, for the first time, reported that microglia in an aggregated state exhibit higher EphA7 expression. EphA7, a member of the Eph receptor family, is well-known for its expression in neurons and its critical role in neuronal growth, differentiation, and synaptic connections [20]. It is involved in neuron-related biological behavior, such as axon guidance [21, 22], synaptic organization, and cortical dendritic development. EphA7 has not been reported to play important physiological functions in microglia. However, there is evidence that EphA2, another Eph receptor, is expressed in microglia and activates the EphA2/p38 MAPK pathway, promoting M1-type polarization, accompanied by reprogramming from oxidative phosphorylation to glycolysis in AD [23]. EphA7 has structural domains similar to those of EphA2, suggesting it may have comparable functions in microglia. Since our sequencing was initially conducted in the cortex and we have established the relationship between tRF$^{Ala-AGC-3-M8}$ and EphA7, we hypothesized that the expression of EphA7 in the cerebral cortex would be abnormally distributed due to the reduction of tRF$^{Ala-AGC-3-M8}$. labeling of Iba1$^+$ /EphA7$^+$ cell in the APP/PS1 transgenic mice brain confirmed this hypothesis. The cerebral cortex of APP/PS1 mice exhibited aggregated microglia, and these aggregated microglia significantly expressed EphA7.

The DG-specific upregulation of EphA7 may be closely associated with the DG region's heightened sensitivity to Aβ toxicity. We subsequently examined EphA7 expression in hippocampal sections. Interestingly, EphA7 was highly expressed in DG neurons. Emerging evidence suggests that DG neurons exhibit increased vulnerability to Aβ-induced synaptic dysfunction and cell death compared to other hippocampal subregions [24]. This selective vulnerability may drive the specific upregulation of EphA7 as a potential protective response or pathological marker. The observed expression pattern could reflect either a compensatory mechanism to counteract Aβ toxicity or an indicator of early pathological changes, given that EphA7 is known to regulate synaptic plasticity and neuronal survival. This region-specific response highlights the DG's unique position in AD progression and suggests that EphA7 may serve as a key mediator in the differential response to Aβ toxicity across hippocampal subregions.

The downregulation of $tRF^{Ala\text{-}AGC\text{-}3\text{-}M8}$ provides another clear pathway to elucidate the toxic effects caused by Aβ deposition. $tRF^{Ala\text{-}AGC\text{-}3\text{-}M8}$ belongs to the tRF-5 category, which is primarily derived from the 5' end of mature tRNA. Studies have shown that cellular stress, such as oxidative stress, hypoxia, and viral infections, can induce the generation of tRF-5 [25–29]. Similarly, The APP/PS1 transgenic mice carry mutant human APP and PS1 genes that promote excessive Aβ aggregation in the brain, leading to amyloid plaque deposition in the cerebral cortex and hippocampus, which subsequently triggers neurotoxic responses. These stresses may cause cells to modulate the expression of tRF-5, especially $tRF^{Ala\text{-}AGC\text{-}3\text{-}M8}$. Our in vitro experiments provide compelling evidence that the reduction of $tRF^{Ala\text{-}AGC\text{-}3\text{-}M8}$ is directly associated with Aβ-induced neurotoxicity. The temporal dynamics of $tRF^{Ala\text{-}AGC\text{-}3\text{-}M8}$ downregulation in HT22 and BV-2 cells reveal a cell-type specific response to Aβ exposure. The earlier downregulation observed in HT22 cells suggests that neurons may be more vulnerable to Aβ toxicity compared to microglia, consistent with previous reports of neuronal susceptibility to Aβ-induced stress [30]. The differential response between BV-2 and HT22 cells can be explained by the inherent capacity of microglia to mitigate Aβ toxicity through phagocytic activity. Our findings support the hypothesis that microglia maintain $tRF^{Ala\text{-}AGC\text{-}3\text{-}M8}$ levels through active Aβ clearance during the initial phase of Aβ exposure (24–36 h). However, prolonged Aβ stimulation ultimately overwhelms the microglial defense mechanisms, leading to cellular dysfunction and significant $tRF^{Ala\text{-}AGC\text{-}3\text{-}M8}$ reduction. This biphasic response pattern suggests that $tRF^{Ala\text{-}AGC\text{-}3\text{-}M8}$ may serve as a sensitive indicator of cellular stress response capacity.

We propose that the interaction between $tRF^{Ala\text{-}AGC\text{-}3\text{-}M8}$ /EphA7 axis holds significant implications in the clinical diagnosis and treatment of AD. Dysregulated tsRNA expression has been linked to various diseases. For instance, the level of $tRF^{His\text{-}GTG\text{-}1}$ positively correlates with neutrophil extracellular traps (NETs) formation in patients with systemic lupus erythematosus (SLE), and $tRF^{His\text{-}GTG\text{-}1}$ inhibitors effectively suppress IC-induced NETs formation and hyperactivation, alleviating symptoms in patients with SLE [31]. Additionally, $tiRNA^{Val\text{-}CAC\text{-}2}$ has been shown to interact with far upstream element-binding protein 1 (FUBP1), stabilizing the FUBP1 protein and increasing its enrichment at the c-MYC promoter region, thereby promoting c-MYC transcription and facilitating pancreatic cancer metastasis [32]. These findings highlight the potential of tsRNAs in disease modulation and underscore the importance of exploring their roles in neurodegenerative diseases like AD. In our study, we systematically analyzed the target genes of $tRF^{Ala\text{-}AGC\text{-}3\text{-}M8}$ using bioinformatics approaches, revealing significant enrichment in critical biological processes such as axon guidance and synaptic organization, with EphA7 emerging as a central player. Subsequent in vitro validation demonstrated that EphA7 exerts profound effects on key cells of the nervous system, including microglia and neurons, through the $ERK_{1/2}$-p70S6K signaling pathway. Current research indicates that the Eph receptor family, including EphA7, influences neurodegenerative disease progression through diverse biological mechanisms. For instance, EphA7 regulates dendritic arborization and spine complexity via Src kinase and the mTOR regulator Tsc1 [33]. Overexpression of EphA7 reduces dendritic branching, while its suppression enhances dendritic complexity and synaptic function. Although direct evidence linking the EphA7-$ERK_{1/2}$-p70S6K signaling pathway to AD pathogenesis is still limited, EphA7 is recognized as a critical mediator of $ERK_{1/2}$ activation [34]. $ERK_{1/2}$ can phosphorylate p70S6K at the T421 and S424 sites, significantly regulating tau protein phosphorylation [35]. Furthermore, p70S6K regulates the expression of cytokines (e.g., IL-6 and TNF-α) and chemokines (e.g., CCL2), as well as transcription factors, such as NF-κB, playing roles in inflammation [36]. Our findings provide compelling evidence that Aβ stimulation downregulates $tRF^{Ala\text{-}AGC\text{-}3\text{-}M8}$ expression, leading to aberrant EphA7 expression in hippocampal neurons and activated microglia. This dysregulation enhances phosphorylation of $ERK_{1/2}$ and p70S6K at T421 and S424 sites, driving pathological processes such as excessive tau phosphorylation and heightened inflammatory responses, ultimately exacerbating neuronal damage in AD. Importantly, our study identifies the EphA7-$ERK_{1/2}$-p70S6K signaling pathway as a novel therapeutic axis that can be targeted for clinical translation. By modulating this pathway, we propose that the detrimental effects of $tRF^{Ala\text{-}AGC\text{-}3\text{-}M8}$ dysregulation in AD could be mitigated, offering a promising strategy for therapeutic intervention.

Conclusions

This study is the first to confirm that $tRF^{Ala\text{-}AGC\text{-}3\text{-}M8}$ plays a role of Aβ toxicity in AD pathology by regulating EphA7, elucidating its specific mechanisms. This finding is significant for the development of novel therapeutic drugs and the prediction of novel diagnostic biomarkers for AD. Nonetheless, our study has certain limitations.

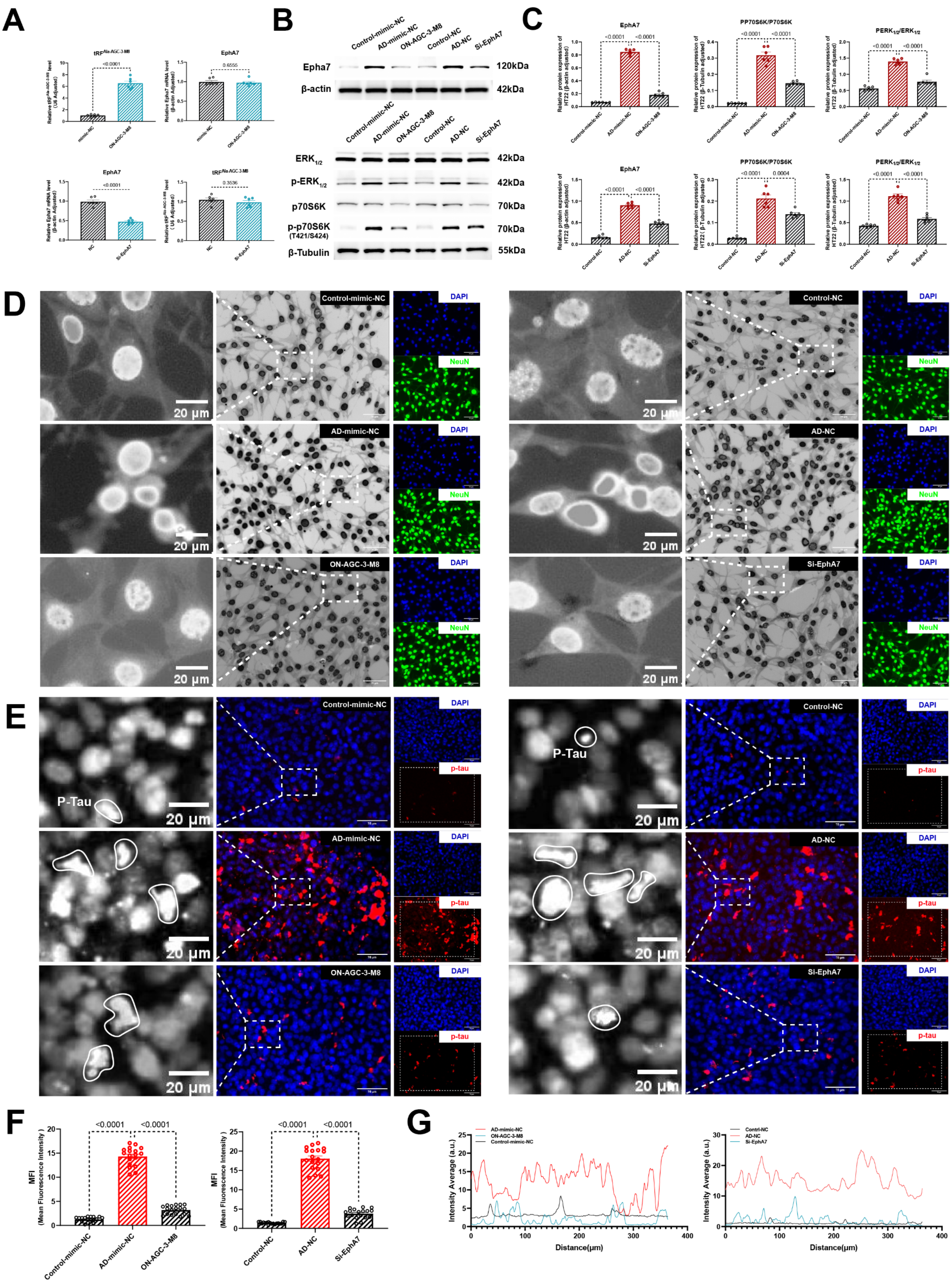

Fig. 9 (See legend on next page.)

(See figure on previous page.)

Fig. 9 Effects of tRF$^{Ala-AGC-3-M8}$ on ERK$_{1/2}$-p70S6K pathway in HT22 cells. **(A)** qRT-PCR analysis of tRF$^{Ala-AGC-3-M8}$ and EphA7 in HT22 cells after transfected with tRF$^{Ala-AGC-3-M8}$-mimic or EphA7-siRNA (*n* = 6, biologically independent samples). **(B-C)** Western blot analysis of EphA7 expression and phosphorylation levels of ERK$_{1/2}$ and p70S6K (T421/S424) (*n* = 6, biologically independent samples). **(D)** Representative image of HT22 morphological features; Scale bar: 75μm (overview), 20μm (insert). **(E, F, G)** Immunofluorescence localization and mean fluorescence intensity of p-tau (Red) in HT22 cells (*n* = 6, biologically independent samples), p-tau was labelled with solid white line in zoomed-in immunofluorescence image; Scale bar: 75μm (overview), 20μm (insert); Statistical significance was assessed using Student's test (A) and one-way ANOVA (C and F) (P values are indicated). All data are presented as the means ± SEM. Each data point represents the average of 3 technical replicates

We propose that changes in tRF$^{Ala-AGC-3-M8}$ expression in AD are dynamic, especially in microglia undergoing polarization and morphological changes. A sustained reduction in tRF$^{Ala-AGC-3-M8}$ may indicate a state where microglia can no longer resist Aβ stimulation. Moreover, since tRF$^{Ala-AGC-3-M8}$ is commonly dysregulated in both neurons and microglia, it might play a significant role as a communication molecule in the crosstalk between neurons and microglia in the hippocampal DG in AD. Further experimental data are required to demonstrate the changes and specific causes of tRF$^{Ala-AGC-3-M8}$ under Aβ stimulation. Addressing these issues will enhance our understanding of the mechanism of action of tRF$^{Ala-AGC-3-M8}$.

Abbreviations

3' UTR	3' Untranslated Region
AD	Alzheimer's Disease
APP/PS1	Amyloid Precursor Protein / Presenilin 1
Aβ	β-amyloid
DG	Dentate gyrus
DMEM	Dulbecco's Modified Eagle Medium
D-tRF	Differentially expressed tsRNAs
Eph	Erythropoietin-producing hepatocellular
Epha7-siRNA	Epha7-targeting siRNA
GO	Gene Ontology
IF	Immunofluorescence
KEGG	Kyoto Encyclopedia of Genes and Genomes
MUT	Mutant Type
NC-mimic	Non-Specific Control mimic
NC-siRNA	Non-Specific Control siRNA
NETs	Neutrophil Extracellular Traps
NFTs	Neurofibrillary Tangles
FBS	Fetal Bovin Serum
FUBP1	Far Upstream Element-Binding Protein 1
PBS	Phosphate-Buffered Saline
qRT-PCR	Quantitative Reverse Transcription Polymerase Chain Reaction
tiRNAs	tRNA-Derived Stress-induced RNA
tRFs	tRNA-Derived Fragments
tRF$^{Ala-AGC-3-M8}$ -mimic	Double-Stranded tRF$^{Ala-AGC-3-M8}$ Mimic
tsRNAs	transfer RNA(tRNA)-derived small RNAs
WB	Western Blotting
WT	Wild Type

Supplementary Information

The online version contains supplementary material available at https://doi.org/10.1186/s13195-025-01734-6.

Supplementary Material 1

Acknowledgements

We extend our sincere thanks to our colleagues and collaborators for their invaluable support and insightful feedback throughout this project. Special appreciation goes to the funding and support provided by the Science and Technology Project of Shenzhen (JCYJ20210324131614038), Guangdong Provincial Basic and Applied Basic Research Foundation (2021A1515220074) and the Shenzhen Key Medical Discipline Construction Fund (SZXK074). Their financial assistance made this work possible.

Author contributions

Li Ling and Fangming Li offered resources, supervision, and funding acquisition throughout the study. Zihao Deng and Yudi Li organized the study and performed the experiments. Conceptualization, methodology, investigation, writing– Original Draft, and visualization were completed by Zihao Deng. Wenjun Chi and Wanzhou Zhang provided technical support and conducted data curation throughout the study. All authors reviewed and approved the final version of the manuscript.

Funding

This study was supported by the Science and Technology Project of Shenzhen (JCYJ20210324131614038), Guangdong Provincial Basic and Applied Basic Research Fundation (2021A1515220074) and the Shenzhen Key Medical Discipline Construction Fund (SZXK074).

Data availability

No datasets were generated or analysed during the current study.

Declarations

Ethics approval and consent to participate

All animal experiments were approved by the Animal Care Ethics Committee of Southern Medical University Shenzhen Clinical Medical College (Resolution No. 2024 – 0184).

Consent for publication

The authors declare that all participants in this study have provided informed consent for the publication of anonymized data, images, and relevant materials collected during the research. The consent process was conducted in accordance with ethical guidelines and institutional policies, ensuring that participants understood the nature of the study and the use of their data in scientific publications. By agreeing to participate in the study, participants consented to the use of their data in the described manner. The authors have ensured that all ethical standards, including confidentiality and respect for participants' rights, have been maintained throughout the research and publication process.

Competing interests

The authors declare no competing interests.

Author details

[1]Department of Neurology, Shenzhen Hospital, Southern Medical University, Shenzhen 518000, China
[2]The First School of Clinical Medicine, Southern Medical University, Guangzhou 510000, China
[3]The Third School of Clinical Medicine, Southern Medical University, Guangzhou 510000, China
[4]Shenzhen Clinical Medical School, Southern Medical University, 518000 Shenzhen, China
[5]Department of Neurology, Clinical Medical Academy, Shenzhen University General Hospital, Shenzhen University, Shenzhen 518000, China

Received: 12 January 2025 / Accepted: 6 April 2025

Published online: 15 May 2025

References

1. Dionisio-Santos DA, Olschowka JA. O'Banion, *Exploiting microglial and peripheral immune cell crosstalk to treat Alzheimer's disease*. J Neuroinflammation. 2019;16(1):74.
2. Gao C, et al. Microglia in neurodegenerative diseases: mechanism and potential therapeutic targets. Signal Transduct Target Ther. 2023;8(1):359.
3. Zheng C, Zhou XW, Wang JZ. The dual roles of cytokines in Alzheimer's disease: update on interleukins, TNF-alpha, TGF-beta and IFN-gamma. Transl Neurodegener. 2016;5:7.
4. Didonna A. Tau at the interface between neurodegeneration and neuroinflammation. Genes Immun. 2020;21(5):288–300.
5. Klakotskaia D, et al. Memory deficiency, cerebral amyloid angiopathy, and amyloid-β plaques in APP + PS1 double Transgenic rat model of Alzheimer's disease. PLoS ONE. 2018;13(4):e0195469.
6. O'Brien RJ, Wong PC. Amyloid precursor protein processing and Alzheimer's disease. Annu Rev Neurosci. 2011;34:185–204.
7. Shen Y, et al. Transfer RNA-derived fragments and tRNA halves: biogenesis, biological functions and their roles in diseases. J Mol Med (Berl). 2018;96(11):1167–76.
8. Xie Y, et al. Action mechanisms and research methods of tRNA-derived small RNAs. Signal Transduct Target Ther. 2020;5(1):109.
9. Jia Y, Tan W, Zhou Y. Transfer RNA-derived small RNAs: potential applications as novel biomarkers for disease diagnosis and prognosis. Ann Transl Med. 2020;8(17):1092.
10. Lisabeth EM, Falivelli G, Pasquale EB. Eph receptor signaling and Ephrins. Cold Spring Harb Perspect Biol. 2013; 5(9).
11. Vargas LM, et al. Amyloid-β oligomers synaptotoxicity: the emerging role of EphA4/c-Abl signaling in Alzheimer's disease. Biochim Biophys Acta Mol Basis Dis. 2018;1864(4 Pt A):1148–59.
12. Cisse M, Checler F. Eph receptors: new players in Alzheimer's disease pathogenesis. Neurobiol Dis. 2015;73:137–49.
13. Schoonaert L, et al. Identification and characterization of nanobodies targeting the EphA4 receptor. J Biol Chem. 2017;292(27):11452–65.
14. Fu AK, et al. Blockade of EphA4 signaling ameliorates hippocampal synaptic dysfunctions in mouse models of Alzheimer's disease. Proc Natl Acad Sci U S A. 2014;111(27):9959–64.
15. Cissé M, et al. Reversing EphB2 depletion rescues cognitive functions in alzheimer model. Nature. 2011;469(7328):47–52.
16. Andrade-Guerrero J et al. Alzheimer's Disease: An Updated Overview of Its Genetics. Int J Mol Sci. 2023; 24(4).
17. Kim K, et al. Clinically accurate diagnosis of Alzheimer's disease via multiplexed sensing of core biomarkers in human plasma. Nat Commun. 2020;11(1):119.
18. Zhang L, Liu J, Hou Y. Classification, function, and advances in tsRNA in non-neoplastic diseases. Cell Death Dis. 2023;14(11):748.
19. Dhahbi JM. 5′ tRNA halves: the next generation of immune signaling molecules. Front Immunol. 2015;6:74.
20. Liang LY, et al. Eph receptor signalling: from catalytic to non-catalytic functions. Oncogene. 2019;38(39):6567–84.
21. Zang Y, Chaudhari K, Bashaw GJ. New insights into the molecular mechanisms of axon guidance receptor regulation and signaling. Curr Top Dev Biol. 2021;142:147–96.
22. Russell SA, Bashaw GJ. Axon guidance pathways and the control of gene expression. Dev Dyn. 2018;247(4):571–80.
23. Ma X, et al. Metabolic reprogramming of microglia enhances Proinflammatory cytokine release through EphA2/p38 MAPK pathway in Alzheimer's disease. J Alzheimers Dis. 2022;88(2):771–85.
24. Tamano, H., et al. Preferential neurodegeneration in the dentate gyrus by amyloid β1-42-induced intracellular Zn2+dysregulation and its defense strategy. Mol Neurobiol. 2020;57(4):1875–88.
25. Rashad S, Niizuma K, Tominaga T. tRNA cleavage: a new insight. Neural Regeneration Res. 2020;15(1):47–52.
26. Thompson DM, Parker R. Stressing out over tRNA cleavage. Cell. 2009;138(2):215–9.
27. Honda S, et al. Sex hormone-dependent tRNA halves enhance cell proliferation in breast and prostate cancers. Proc Natl Acad Sci USA. 2015;112(29):E3816–25.
28. Yamasaki S, et al. Angiogenin cleaves tRNA and promotes stress-induced translational repression. J Cell Biol. 2009;185(1):35–42.
29. Cai J, et al. Angiogenin-mediated tsRNAs control inflammation and metabolic disorder by regulating NLRP3 inflammasome. Cell Death Differ. 2024;31(8):1057–69.
30. Guo T, et al. Molecular and cellular mechanisms underlying the pathogenesis of Alzheimer's disease. Mol Neurodegeneration. 2020;15(1):40.
31. Chen YM, et al. tRF-His-GTG-1 enhances NETs formation and interferon-α production in lupus by extracellular vesicle. Cell Commun Signal. 2024;22(1):354.
32. Xiong Q, et al. tiRNA-Val-CAC-2 interacts with FUBP1 to promote pancreatic cancer metastasis by activating c–MYC transcription. Oncogene. 2024;43(17):1274–87.
33. Kania A, Klein R. Mechanisms of ephrin-Eph signalling in development, physiology and disease. Nat Rev Mol Cell Biol. 2016;17(4):240–56.
34. Nakanishi H, et al. ALL1 fusion proteins induce deregulation of EphA7 and ERK phosphorylation in human acute leukemias. Proc Natl Acad Sci U S A. 2007;104(36):14442–7.
35. Zhou XW, Tanila H, Pei JJ. Parallel increase in p70 kinase activation and Tau phosphorylation (S262) with Abeta overproduction. FEBS Lett. 2008;582(2):159–64.
36. Lin CH, et al. Mammalian target of Rapamycin and p70S6K mediate thrombin-induced nuclear factor-κB activation and IL-8/CXCL8 release in human lung epithelial cells. Eur J Pharmacol. 2020;868:172879.

Publisher's note

Springer Nature remains neutral with regard to jurisdictional claims in published maps and institutional affiliations.